Research article

Shuo Du, Zhe Liu, Chi Sun, Wei Zhu, Guangzhou Geng, Haitao Ye, Junjie Li* and Changzhi Gu*

Cross-nanofin-based waveplate pixels for broadband hybrid polarization coding in near-field

https://doi.org/10.1515/nanoph-2020-0621
Received November 23, 2020; accepted January 21, 2021; published online February 23, 2021

Abstract: As an inherent characteristic of light, polarization plays important roles in information storage, display and even encryption. Metasurfaces, composed of specifically designed subwavelength units in a two-dimensional plane, offer a great convenience for polarization manipulation, yet improving their integrability and broadband fidelity remain significant challenges. Here, based on the combination of various subwavelength cross-nanofins (CNs), a new type of metasurface for multichannel hybrid polarization distribution in near-field is proposed. Sub-wavelength CN units with various waveplate (WP) functionalities, such as frequency-division multiplexing WP, half-WP and quarter-WP are implemented with high efficiency in broadband. High-resolution grayscale image encryption, multi-image storage and rapid polarization detection are demonstrated by encoding the WP pixels into single, double and four channels, respectively. All these applications possess good fidelity in an ultrabroad wavelength band from 1.2 to 1.9 μm, and the high degree of integrability, easy fabrication and multifunction make the CN-shaped WP pixels a promising candidate in optical device miniaturization, quantum applications and imaging technologies.

Keywords: broadband and high-efficiency metasurface; high-resolution grayscale image; multi-image storage; rapid polarization detection; subwavelength waveplate pixels.

Shuo Du and **Zhe Liu** are contributed equally to this work.

***Corresponding authors: Junjie Li**, Beijing National Laboratory for Condensed Matter Physics, Institute of Physics, Chinese Academy of Sciences, Beijing 100190, China; and Songshan Lake Materials Laboratory, Dongguan, Guangdong 523808, China; and **Changzhi Gu**, Beijing National Laboratory for Condensed Matter Physics, Institute of Physics, Chinese Academy of Sciences, Beijing 100190, China; and School of Physical Sciences, CAS Key Laboratory of Vacuum Physics, University of Chinese Academy of Sciences, Beijing 100049, China, E-mail: jjli@iphy.ac.cn (J. Li), czgu@iphy.ac.cn (C. Gu)

Shuo Du and Chi Sun, Beijing National Laboratory for Condensed Matter Physics, Institute of Physics, Chinese Academy of Sciences, Beijing 100190, China; CAS Key Laboratory of Vacuum Physics, School of Physical Sciences, University of Chinese Academy of Sciences, Beijing 100049, China. https://orcid.org/0000-0003-4027-5167 (S. Du)

Zhe Liu, Center for Hybrid Quantum Networks (Hy-Q), Niels Bohr Institute, University of Copenhagen, Blegdamsvej 17, DK-2100 Copenhagen, Denmark

Wei Zhu and Guangzhou Geng, Beijing National Laboratory for Condensed Matter Physics, Institute of Physics, Chinese Academy of Sciences, Beijing 100190, China. https://orcid.org/0000-0003-0673-3048 (W. Zhu)

Haitao Ye, Department of Engineering, University of Leicester, Leicester LE17RH, UK

1 Introduction

In the last decade, metasurfaces are of great interest in optical researches [1, 2]. It offers abundant possibilities to store, hide or encrypt information because of its powerful capability for light manipulation. The wavelength, amplitude, propagation angle, and even direction, all these parameters of light can be modulated by metasurfaces, and meanwhile, the capacity of metadevices can be easily enhanced by plenty of multiplexing strategies based on these parameters [3–8]. As another fundamental nature of light, polarization is not only a great source of information (material properties, optical activity and quantum information) but also a significant degree of freedom to control light [9, 10]. Thus the polarization manipulation and multiplexing have long been hotspots in metasurface study. By the superposition of two circularly polarized light beams with opposite handedness based on a single metallic metasurface, the high-resolution grayscale images carried by space-variant linear polarization (LP) profile can be stored in a laser beam [11–13], which has fascinating applications in areas such as anticounterfeiting and information

Open Access. © 2021 Shuo Du et al., published by De Gruyter. This work is licensed under the Creative Commons Attribution 4.0 International License.

encryption. With the high precision of the reconstructed images, metasurface holography is another important means for image storage [14, 15]. With the feature of less crosstalk and multichannel, polarization multiplexing has been widely utilized to enhance the capacity of holographic metasurfaces [16–18], which holds great potential in massive information storage and holographic data encryption. However, in order to obtain a good image quality and avoid cross-talk from input light, most of these works are designed to be an off-axis configuration or require a relatively longer diffraction distance, hence extra space is needed in the device for data readout, which is not compatible or difficult to integrate with the existing photosensitive elements [19], such as charge-coupled device (CCD) or complementary metal oxide semiconductor (CMOS), by direct on-chip manufacturing.

All-dielectric nano-waveplates (nano-WPs) exhibit excellent capability for polarization conversion in subwavelength local near-field [20]. They overcome the disadvantages of traditional WPs' large volume, such that they can be integrated with imaging sensors easily [19]. However, the potential of using nano-WPs for near-field information manipulation, such as image encryption, multichannel storage, has not been explored. In this work, we propose a series of cross-nanofin (CN)-shaped subwavelength WPs, which can serve as coding pixels to constitute an all-silicon metasurface with multiple hybrid polarization distributions in near-field. As the schematic illustration shows in Figure 1(a), each nanoscale CN unit manipulates the local polarization state individually and functions as a specific miniaturized WP, such as half-waveplate (HWP), positive and negative quarter-waveplates (±QWP), with the features of broadband and frequency-division multiplexing (FDM). From Figure 1(a)–(d), the output polarization in near-field of each subwavelength pixel can be determined by the polarization conversion feature of each CN, and it is dynamically switched by tailoring the input polarization (the number of multiplexing channels can be increased by introducing other phase retarder pixels). These characteristics enable our metasurface with the ability to manipulate information: a high-resolution grayscale image with pixels per inch (ppi) reaching 35,219, is stored and encrypted in a complex near-field hybrid polarization profile generated by a combination of different types of CN units; multiple images of alphabets or QR-codes can be encoded in different output near-field polarization profiles on a single metasurface by polarization multiplexing. Besides, such all-silicon configuration has extra degrees of design freedom in frequency multiplexing,

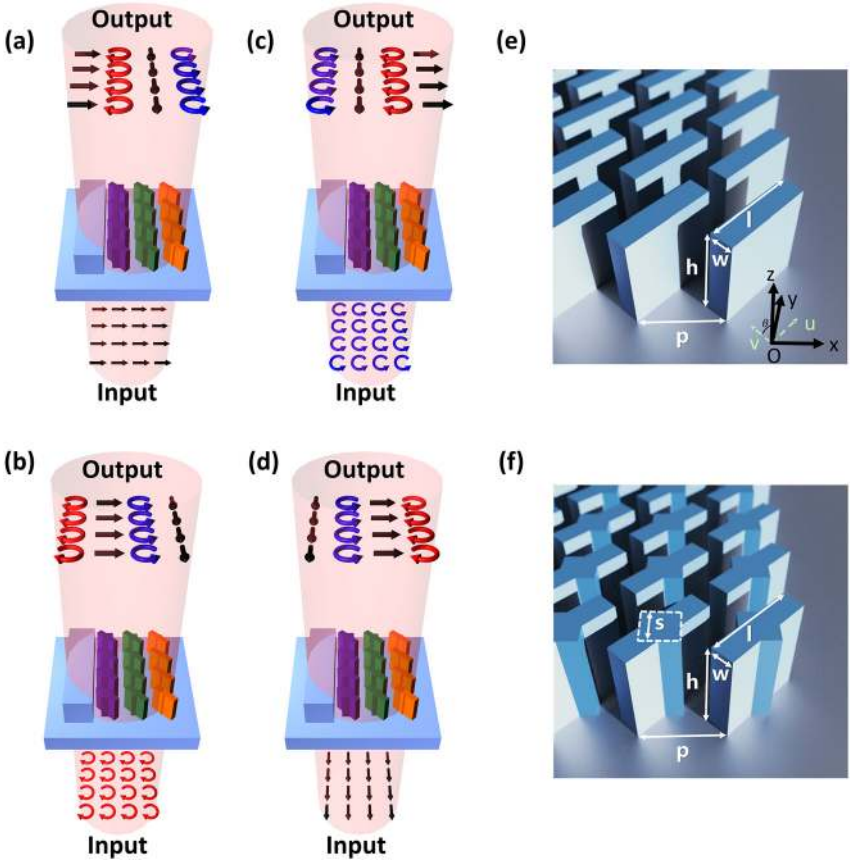

Figure 1: Schematic illustrations of CN–based metasurfaces.
(a)–(d) Dynamic modulation of hybrid polarization distribution by switching the input polarization among *x*-LP, *y*-LP, left circular polarization (LCP) and right circular polarization (RCP). From left to right, the blue cuboid structure does not convert the input polarization; the purple CNs function as +QWP; the green CNs function as HWP; the orange CNs function as −QWP. (e) Schematic of conventional cuboid nanofin array. (f) Schematic of CN array.

and can be direct integration onto existing imaging sensors due to its near-field manipulation, holding great promise for information storage, rapid polarization detection and quantum applications.

2 Design of cross-nanofin

Conventional dielectric cuboid nanofin array with HWP functionality [21] is shown in Figure 1(e). The underlying physics of polarization conversion is similar to birefringent crystal. It provides a phase difference between two orthogonally polarized wave components of transmitted light in an ultrashort distance. The long and short axes of nanofins are parallel to u and v axis which is rotated 45° compared to x and y axes, therefore it's much easier to discuss the relationship between different polarization components in the uOv coordinate. The transmission matrix T^{uv} can be written as:

$$T^{uv} = \begin{pmatrix} t_{uu} & t_{vu} \\ t_{uv} & t_{vv} \end{pmatrix} \tag{1}$$

Due to the symmetry along u/v axes, there are no cross-polarization terms which means the counter-diagonal elements are zero. The intensity of t_{uu} and t_{vv} are both close to 1.0 because of the low loss of dielectric material, and the phase difference can be expressed based on the effective indices of transmission modes along the two axes:

$$T^{uv} = t_{uu}\begin{pmatrix} 1 & 0 \\ 0 & e^{i(n_v - n_u)\omega z/c} \end{pmatrix} \tag{2}$$

Here, t_{vv} is expressed by a phase change of t_{uu}. Without loss of generality, t_{uu} can be taken as 1 to remove the phase term, which will not cause any ambiguities in the following analysis. The transmission matrix T^{xy} along x and y axis can be calculated through the rotation matrix $R(\theta)$ in the form of:

$$\begin{aligned} T^{xy} &= R\left(-\frac{\pi}{4}\right)\begin{pmatrix} 1 & 0 \\ 0 & e^{i(n_v - n_u)\omega z/c} \end{pmatrix} R\left(\frac{\pi}{4}\right) \\ &= \frac{1}{2}\begin{pmatrix} 1 + e^{i(n_v - n_u)\omega z/c} & -1 + e^{i(n_v - n_u)\omega z/c} \\ -1 + e^{i(n_v - n_u)\omega z/c} & 1 + e^{i(n_v - n_u)\omega z/c} \end{pmatrix} \end{aligned} \tag{3}$$

which represents the property of nanofin metasurface connecting polarized incident and transmitted light. In two special cases, it operates as functional WPs:

(1) When n_v and n_u meet the following relation:

$$(n_v - n_u)\omega z/z = \pm(2n+1)\pi, n = 0, 1, 2, \ldots$$

the metasurface plays a role of HWP that it can rotate the linearly polarized input light with an angle of 90°, or invert the handness of circular or elliptically polarized input light (see Section S1 and S2, Supporting Information).

(1) When the following relation is satisfied

$$(n_v - n_u)\omega z/z = \pm(2n+1)\pi/2, n = 0, 1, 2, \ldots$$

the metasurface operates as QWP, that when the incident light is linearly/circularly polarized, the transmitted light is converted to circularly/linearly polarized light, respectively (see Section S3, Supporting Information).

The mechanism of the interaction between light and high-aspect ratio nanofins is high-order multi-waveguide mode [21], and the modulation of phase difference can be achieved by changing either the structure size (e.g., the length of the long axis $\boldsymbol{l}$ [22]) or geometrical shapes [23, 24]. Here, in order to have an effective control of nanofins, both size and shape are changed by combining the cuboid nanofin with a rectangular pillar with a side length of $\boldsymbol{s}$ to form a composite CN shape configuration, as shown in Figure 1(f). By tailoring size $\boldsymbol{s}$, versatile types of broadband WPs can be implemented.

The numerical simulation and measured intensity transmissivity spectra of different CN arrays (p = 1.2 μm, h = 2 μm, w = 0.34 μm, l = 1.36 μm and $\boldsymbol{s}$ varies from 0 to 650 nm) are shown in Figure 2(a) and (b), and all the different CN arrays are illuminated vertically by x-polarized LP light. T_{yx} and T_{xx} represent the transmissivity of cross- and copolarized transmitted energy, and $T_{yx} = |t_{yx}|^2$, $T_{xx} = |t_{xx}|^2$, where t_{yx} and t_{xx} are elements of Jones matrix T_{lin} in Equation (S1). The SEM images of corresponding CNs with s varying from 0 nm (conventional cuboid nanofin) to 650 nm are shown in Figure 2(c). During the changing of s, the variation of T_{yx} and T_{xx} reveals the information of phase difference [22], WP type, working bandwidth and efficiency intuitively.

When s is 0 nm, the magnitude of T_{yx} overwhelms T_{xx} from 70 to 100 THz, indicating that the x-polarized incident light is mainly converted to y-polarized light. Especially, the x component is close to zero from 90 to 95 THz, which is in the band named "high-efficiency HWP band" (see Figure 2(a), from around 70 to 100 THz). With s increasing from 0 to 500 nm, the relation between T_{yx} and T_{xx} in this "high-efficiency HWP band" remains unchanged, but it varies in the higher frequency band from 110 to 140 THz which is named as "functionality changing band". This is a valuable feature, which makes broadband FDM WP and ultra-broadband HWP possible.

When s is 350 nm, T_{yx} and T_{xx} are very close in the "functionality changing band", which indicates that the QWP functionality appears in such a broad frequency band (phase relation between t_{yx} and t_{xx} are not shown here but

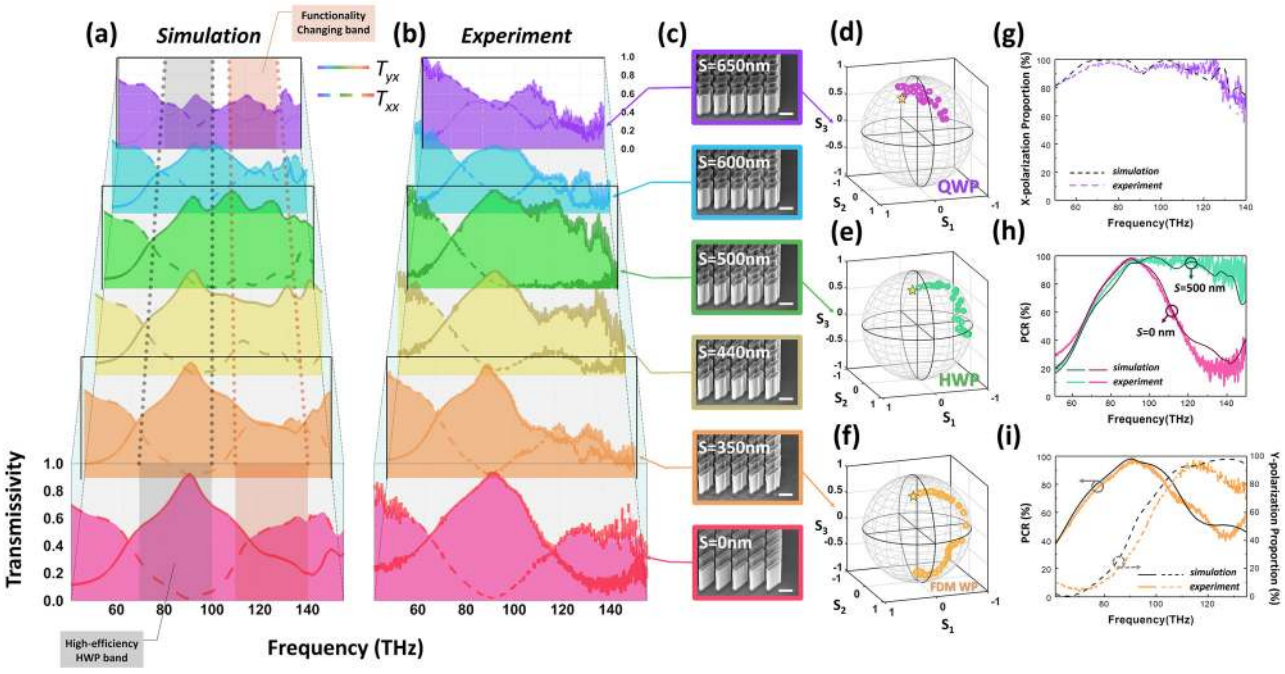

Figure 2: Polarization manipulation performance of different CNs.
(a) and (b) Numerical simulated and experimentally measured intensity transmissivity spectra of different CN metasurfaces. (c) SEM images of CN metasurfaces with s varies from 0 to 650 nm. (d)–(f) Poincaré spheres of output light for x-polarized input of CN when s = 650, 500 and 350 nm. (g) Simulated (black dash curve) and measured (violet dash curve) proportion of y-polarized light in the transmitted field when s = 650 nm. (h) Simulated and measured PCR of CN when s = 0 nm (dark red and light red curves) and s = 500 nm (dark green and light green curves). (i) Simulated (black curves) and measured (orange curves) PCR (solid line) and proportion of y-polarized light in the transmitted field (dash line) when s = 350 nm.

can be proved by Poincaré spheres later), hence the CNs possess the feature of QWP and HWP simultaneously. With s further increasing to 500 nm, the T_{yx} overwhelms T_{xx} largely in the "functionality changing band", where the transmitted light is mainly y-polarized from 70 to 150 THz, therefore an ultrabroadband HWP is generated. As s continuously increases to 650 nm, the magnitude of T_{yx} drops and T_{xx} increases, and eventually they are closer to each other in the entire frequency band from 70 to 150 THz, which indicates the generation of ultra-broadband QWP (strictly speaking, at some points T_{yx} and T_{xx} are not exactly equal thus elliptical polarization can be get from this QWP). In general, with the increasing of s, the functionality of CN is transformed from HWP (0 nm) to FDM WP (350 nm), ultra-broadband HWP (500 nm), and finally ultra-broadband QWP (650 nm).

To further characterize the polarization conversion performance, Poincaré spheres of three representative CNs are presented in Figure 2(d)–(f), on which the transmission behavior of WPs with x-polarized incidence can be tracked. The north/south pole of the sphere represents LCP/RCP transmission, and the intersections between equator and S1 axis represent x- (positive) and y- (negative) polarized transmission. The paths on the sphere illustrate the transmitted polarization states in the frequency range from 60 (marked as a star) to 140 THz.

2.1 FDM-CN

In the case of s = 350 nm, as shown in Figure 2(f), the WP has three functionalities in different frequency bands—two types of QWP and one HWP. The polarization conversion ratio (PCR) is defined to demonstrate the efficiency of HWP (due to structure symmetry, the conversion ability for LP and CP wave is the same):

$$\mathrm{PCR} = \frac{|t_{yx}|^2}{(|t_{yx}|^2 + |t_{xx}|^2)} = \frac{|t_{RL}|^2}{(|t_{RL}|^2 + |t_{LL}|^2)} \tag{4}$$

where t_{RL} and t_{LL} are elements of Jones matrix T_{circ} in Equation (S2). As shown in Figure 2(i), the high efficiency working band of HWP where the PCR is higher than 90% ranges from 83.4 to 102 THz in the simulated result, and from 85.5 to 99.3 THz in the measurement.

To characterize the efficiency of QWP, the input source is chosen to be LCP light, and the proportion of y-polarized light

in the transmitted field is calculated, as shown in Figure 2(i) (dashed curves). From 60 to 80 THz, the incident LCP light is mostly converted to *x*-polarized light (*y*-polarization < 10%) in measured results, and this part is the so-called positive QWP (+QWP) [25]. On the contrary, from 110 to 122 THz the measured transmitted light is mainly *y*-polarized (*y*-polarization > 90%), indicating a negative QWP (–QWP). The transition between + QWP and –QWP is because of a π phase difference, which has been explained in Section S3 of Supporting Information. The path on Poincaré sphere in Figure 2(f) also illustrates this transition clearly that when the frequency varies from 60 to 140 THz, the polarization state of transmitted light is transformed from LCP (north pole) to *y*-LP (negative S1 axis), and then RCP (south pole) with *x*-polarized incidence. This proves that the CN at $\boldsymbol{s}$ = 350 nm can operate as positive QWP, HWP and negative QWP simultaneously in different frequency bands.

2.2 HWP-CN

When $\boldsymbol{s}$ = 500 nm, the bandwidth of HWP-feature has an obvious extension compared to that of the original nanofins ($\boldsymbol{s}$ = 0 nm). For comparison, the simulated and measured PCR for both $\boldsymbol{s}$ = 0 nm and $\boldsymbol{s}$ = 500 nm are shown in Figure 2(h). It is evident that, by introducing the additional rectangular pillar, the high efficiency working band of HWP is greatly widened, and the band width where PCR is higher than 90% is 2.5 times (2.6 times) wider than that of $\boldsymbol{s}$ = 0 nm in simulated (experimental) result. The path on Poincaré sphere in Figure 2(e) also shows that the transmitted light is basically converted from x-to y-polarization (negative S1 axis) within that band. The broadband and high efficiency of HWP polarization conversion enables this CN WP great potential to be a geometric phase modulation building block to construct broadband wavefront manipulation metadevices, such as metalens, holography, beam splitter, etc. [21, 26, 27].

2.3 QWP-CN

As far as $\boldsymbol{s}$ = 650 nm, the path on Poincaré sphere in Figure 2(d) shows that the input *x*-polarized light is mostly converted to LCP light (north pole). To further characterize the conversion efficiency, LCP incident light is used, and Figure 2(g) shows that there's a high proportion of *x*-polarized wave in the transmitted light. It is higher than 80% from 50 to 130 THz in both simulated and measured results. This proves that the CN WP at $\boldsymbol{s}$ = 650 nm works as an ultrabroadband +QWP.

In order to elucidate the underlying physics in the process of WP type transformation, each CN is considered as a vertically placed waveguide [23], and the field distributions of CNs at 110 THz are simulated. Figure 3(a)–(c) shows the normalized instantaneous magnetic field strength distributions along the long axes of the CNs when $\boldsymbol{s}$ = 0, 500 and 650 nm, respectively, which are excited by LP wave polarized along the long axes (linear +45° polarization). Besides, the magnetic field strength distributions along the short axes are shown in Figure 3(d)–(f) which are illuminated by LP wave polarized along the short axes (linear –45° polarization). Different waveguide modes can be recognized from the number of nodes in magnetic field distribution [21, 28]. It shows that the modes in long axis of CNs are similar (the numbers of nodes from them are equal), while in short axis, they are quite different, indicating that the additional rectangular column only has great effects on the short axis modes. Therefore, the modulation of phase difference between the two axes is controllable by $\boldsymbol{s}$ parameter. To further illustrate this, we calculated the effective refractive index of long and short axis modes [29] when $\boldsymbol{s}$ = 0, 500 and 650 nm, from 80 to 160 THz. As shown in Figure 3(g), the n_{eff} of short axis modes increases more significantly with the increasing of *s* than that of long axis modes, hence the phase difference between the long and short axes decreases in this band. As calculated in Figure 3(h), the decreased phase difference when *s* = 500 nm maintains close to π from 80 to 130 THz, which is much broader than that when $\boldsymbol{s}$ = 0 nm, implementing the functionality of broadband HWP. When $\boldsymbol{s}$ = 650 nm, the phase difference continues to decrease and is close to $\pi/2$ from 80 to almost 120 THz, realizing the functionality of QWP. Compared with the transmission in free space, the high order transmission mode in the additional rectangular column possesses a larger n_{eff}, from which the CNs get great capability of electromagnetic field confinement and phase retardance, realizing the band broadening for HWP and functionality transforming from HWP to QWP.

In addition, compared with the conventional nanofin structure, the CN structure allows for a larger machining tolerance, especially for the fabrication of FDM WP, and related contents have been added in Section S4 of Supporting Information. Besides, all these types of WPs can be implemented to different sizes or dielectric materials, to meet the demand in different frequency regions (Section S5, Supporting Information).

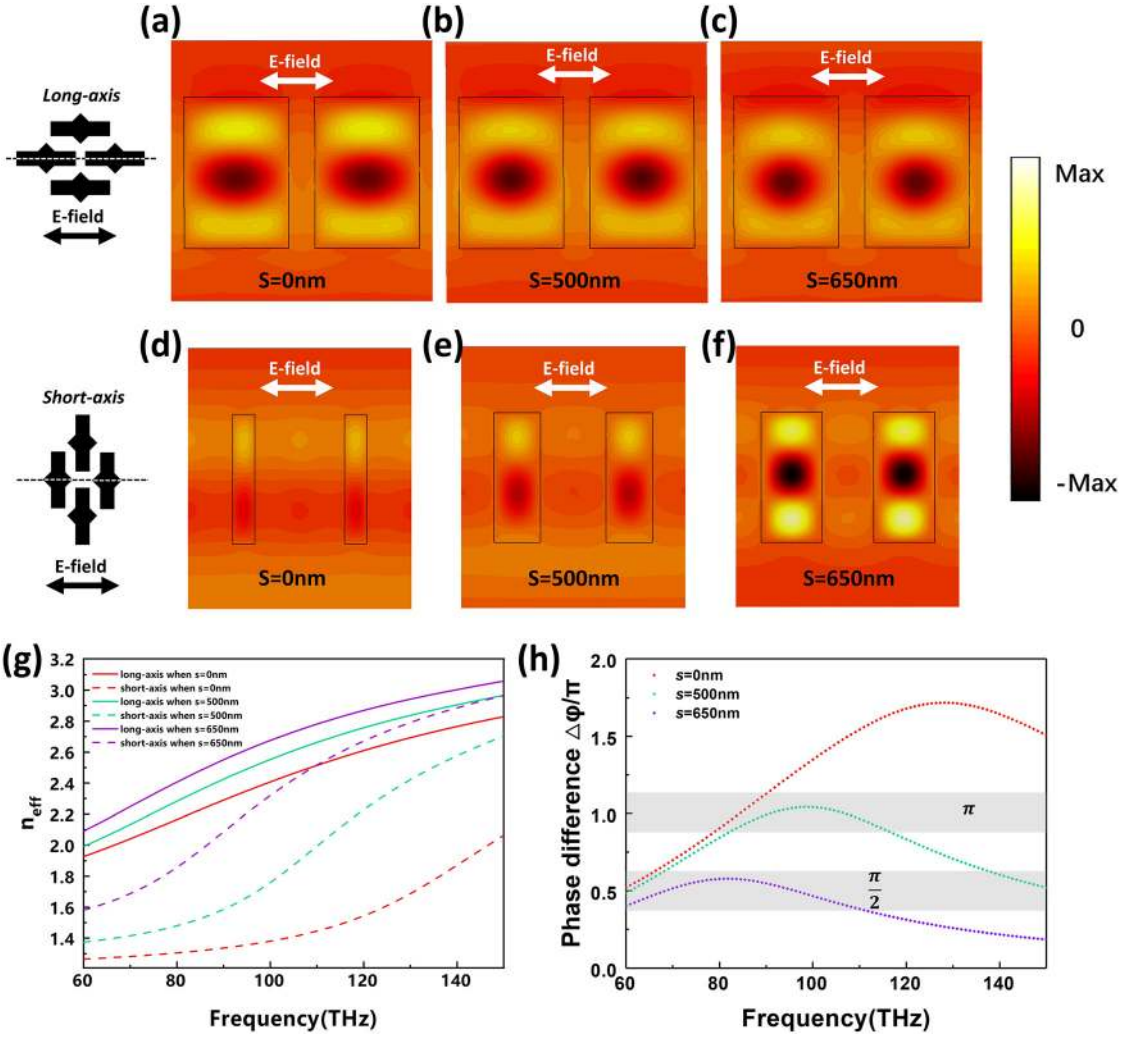

Figure 3: Underlying physics in the process of WP type transformation.
(a)–(c)/(d)–(f) Simulated instantaneous magnetic field strength distributions along the long/short axes of the CNs when s = 0, 500 and 650 nm, respectively. (g) Simulated effective refractive index of polarized incidence along long and short axes when s = 0, 500 and 650 nm. (h) Calculated phase difference between long and short axes when s = 0, 500 and 650 nm.

3 Application of near-field multichannel hybrid polarization

To demonstrate the near-field inhomogeneous distribution of hybrid polarization in a single input polarization channel, CNs with different s are assembled on a single metasurface. Figure 4(a) shows the cross-polarization transmissivity T_{xy} as a function of size s at the wavelength of 1.55 μm, and the CNs are scaled down to 60% of the original size in Figure 2, and that is p = 0.72 μm, h = 1.2 μm, w = 0.204 μm, l = 0.816 and $\boldsymbol{s}$ varies from 0 to 720 nm. The CNs possess the same polarization conversion functionalities in near-infrared (NIR) region, and their transmissivity spectra are shown in Section S6 of Supporting Information. As a simple demonstration, we reconstruct a 2-bit grayscale image of a panda (binary 00 to 11, in Figure 4(b)), and the pixels of this grayscale image are replaced by four types of CNs (Figure 4(c) and (d)). It is hard to figure out the details of the pattern from the SEM image (Figure 4(c)). The local output polarization states of these four types of CNs are shown in Figure 4(a) with y-LP input, and when the sample is observed in NIR (Figure 4(e)), the non-polarized or copolarized transmitted field (Figure 4(f) and (g)) cannot reveal the details of the image. The pattern of panda can only be decrypted in the cross-polarized transmitted field (Figure 4(h)), where the light intensity of those four polarization pixels corresponds to 11, 10, 01 and 00, respectively. The decrypted picture retains all the details compared with the original image, such as panda's tongue, teeth and eyes. Theoretically, the gray-level of encrypted images can be more

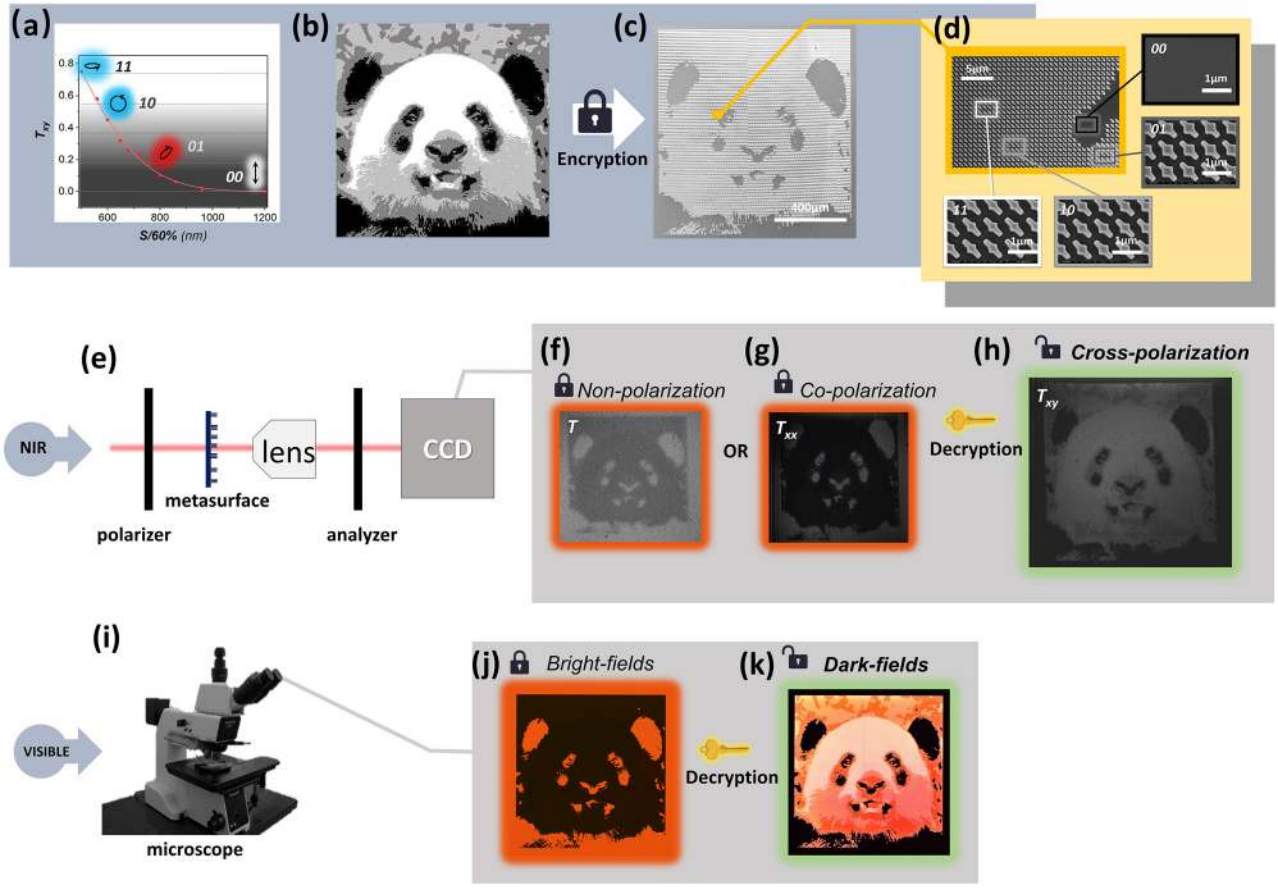

Figure 4: Single-channel image storage for high-resolution grayscale image encryption.
(a) Simulated cross-polarization transmissivities (T_{xy}) of CNs with different ***s***, and the local output polarization of four types of CNs in (d) are also marked. (b) Original 2-bit grayscale image of a panda. (c) SEM image of encrypted metasurface, and it is composed of four kinds of CNs. (d) Enlarged SEM images of the encrypted metasurface in (c), and there are four kinds of CNs in this region. The numbers on the images demonstrate the 00, 01, 10 and 11 grayscale values of the corresponding pixels. (e) Experimental setup to characterize the encrypted image in the band from 1.2 to 1.9 μm. (f)–(h) Infrared microscopic images of the encrypted metasurface observed by unpolarized transmission light, copolarized transmission light and cross-polarized transmission light. (i) Picture of microscope operating in visible band. (j) and (k) Dark-field and bright-field microscopic images of the encrypted metasurface observed in visible band.

finely divided, but for a convenient design, we only divide it into four levels. That may degrade the image quality, but should be enough for principle illustration. Besides, due to the broadband feature of CNs, the grayscale image is observed in a broad working band from 1.2 to 1.9 μm with good fidelity. The subwavelength polarization distribution also enables the recorded image with high resolution, and the size of each pixel in NIR region is 0.7 μm, which is much smaller than the size of CCD pixel (typically 10–20 μm).

Meanwhile, the encrypted information can also be read out in visible band. When the sample is observed under the microscope, as shown in Figure 4(i), the information of image cannot be decrypted by bright-field (Figure 4(j)), but when the directly transmitted light is blocked, the details of panda jump out as Figure 4(h) displays. It should be noted that this intensity profile comes from the higher-order diffraction by the tiny difference of CNs with different ***s***, instead of polarization conversion [30].

As demonstrated in Figure 1(a), the output near-field polarization state of a certain CN unit can be varied by changing the input polarization, which enables the dynamic control of the polarization distribution. In the application of grayscale image encryption, only one polarization distribution (cross-polarization) was used to carry the predesigned information. By selecting the CNs with special functionalities, another polarization distribution of copolarized transmitted light can also serve as an information channel. The CNs in Figure 2(d) to (f) have excellent polarization conversion capabilities, and they function as +QWP, HWP and −QWP, respectively, in broadband. Figure 5(a) shows the ellipticity (S_3/S_0 from Stokes parameters) [25] of these three kinds of CNs (scaled

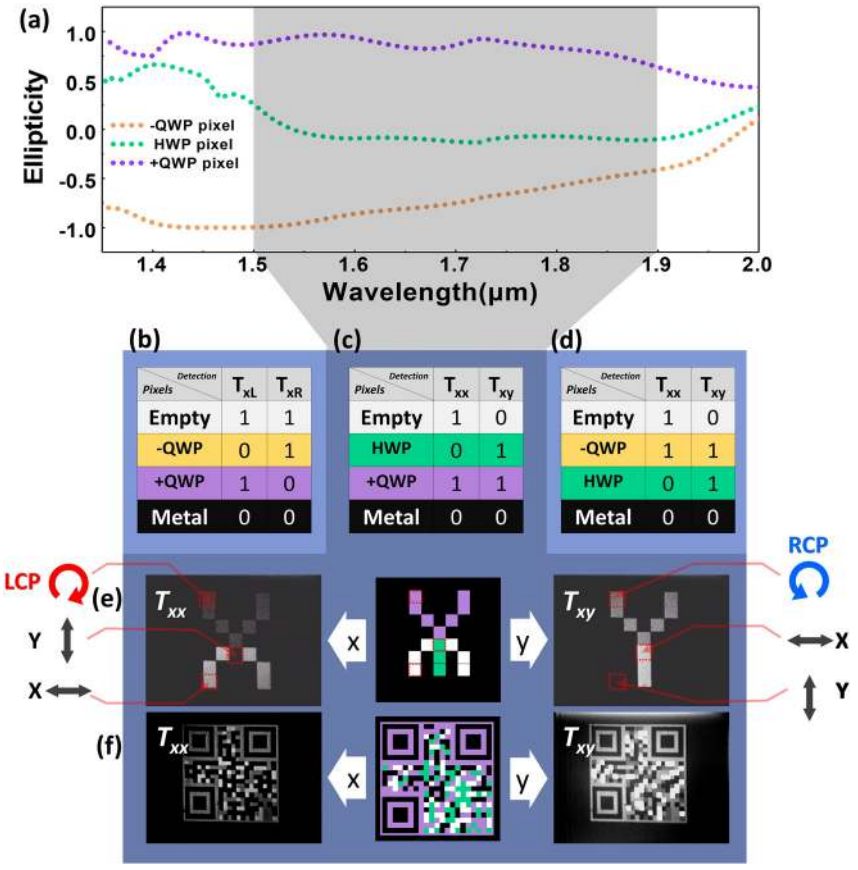

Figure 5: Double channels image storage. (a) Simulated ellipticity of three kinds of CNs. (b)–(d) Encoding tables of double channels image storage. (e) Images of letter "*X*" and "*Y*" are encoded on a single metasurface, and they can be read by co- and cross-polarization transmission light, respectively. The output states in the polarization distributions of the red dotted box areas in the middle schematic illustration are marked in the left and right sides of (e). (f) Images of two completely different QR codes that are encoded on different channels on a single metasurface, and they can be read by co- and cross-polarization, respectively.

down to 60% from CNs with $\boldsymbol{s}$ = 350, 500 and 650 nm for NIR). When the ellipticity equals to 1/–1, LP input can be perfectly converted to LCP/RCP output and vice versa, and when ellipticity is 0, the output is orthogonal polarization. In the range from 1.5 to 1.9 μm, these CNs can convert input *x*-LP light to RCP (with ellipticity ranges from 0.65 to 0.97), *y*-LP (with ellipticity ranges from –0.09 to 0.25) and LCP (with ellipticity ranges from –1 to –0.41). When these states of polarization are observed by an *x*-analyzer, the relative brightness of output light intensity are half-bright, black and half-bright. Meanwhile, when they are observed by *y*-analyzer, the intensities are half-bright, bright and half-bright. If bright/half-bright is taken as 1 and black as 0, three coding tables can be constructed (depicted in Figure 5(b)–(d)). Any one of the three tables constitutes a complete set, which can be used to encode two mutually independent images on a single metasurface. The pixel *Empty* represents blank pixel without CN whose states of output polarization are consistent with input light, and the pixel *Metal* represents opaque metal square, which can block the light and output 0.

The schematic in the middle of Figure 5(e) exhibits the encoding scheme of double channels storage for two independent images of letter "*X*" and "*Y*" on a single metasurface. Different color areas in the schematic represent different kinds of pixels in the code table of Figure 5(c). The left and right images of Figure 5(e) are the stored images read out by copolarization (*x*-LP input) and cross-polarization (*y*-LP input) transmitted setup in a broadband from 1.2 to 1.9 μm, respectively. The hybrid output polarizations are marked on these two intensity images. It can be found that the states of polarization on two output channels are orthogonal, which can largely avoid the cross-talk between channels. As well as the grayscale image encryption, the stored images here also have high resolution. Their ppi reaches 35,219, which is far more than that of typical printer (300–1440 ppi). Figure 5(f) is another example showing that two distinct high-resolution (1000 × 1000) QR codes can be simultaneously stored in an area less than 0.5 square millimeter.

The above realization of double channels image storage only requires two kinds of CNs, and by introducing more types of CNs into the metasurface construction, the number of storage channel can be further extended. By using all the three types of CNs in Figure 5(a), four channels storage is implemented, which can be used for rapid polarization detection. As demonstrated in Figure 5(e), the letters ("*X*"/"*Y*") after x-analyzer represent the linear input polarization type, and with the increasing of the channel

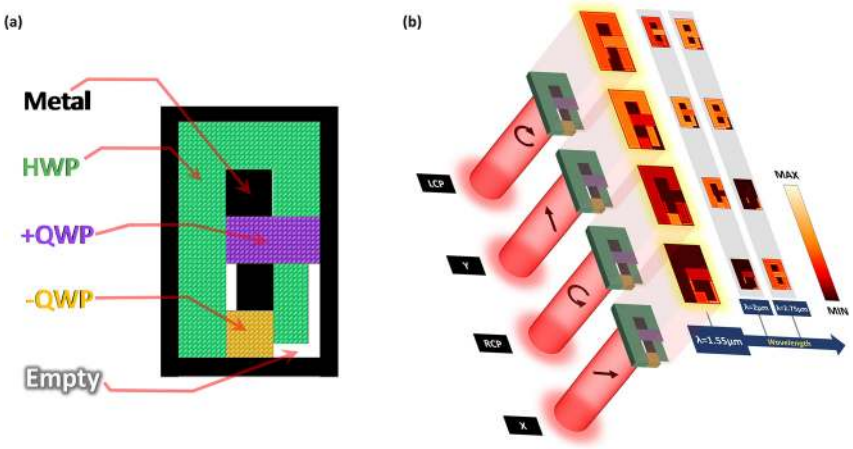

Figure 6: Four channels image storage for rapid polarization detection.
(a) Schematic diagram of CNs arrangement for four input polarization states detection. (b) Simulated *x*-component field distributions from four polarization states input at three frequencies.

number, more states of input polarization can be distinguished. Here, a method for the detection of four input polarization states (LCP, RCP, *x*-LP and *y*-LP) is proposed. The schematic diagram of constructed metasurface is shown in Figure 6(a). When the input polarization varies from LCP to *y*-LP, RCP and finally *x*-LP, the image after *x*-analyzer changes from letter "*A*" to "*B*", "*C*" and finally "*D*" (Figure 6(b)). Conventional method for detecting these four polarization states requires two steps by using a polarizer and a QWP. Compared with that, our strategy can be faster and more convenient, since the input polarization can be distinguished by visual inspection in one step immediately.

Moreover, because of the FDM feature of CNs, the wavelength of input light can be another degree of freedom for the output hybrid polarization manipulation. When the ellipticity of CNs in Figure 5(a) are calculated to the wavelength of 2.9 μm (Section S7, Supporting Information), these three CNs almost all work as HWP at 2 μm, and +QWP at 2.75 μm. Figure 6(b) gives the output image variation from wavelength around 1.55 μm ("*A*", "*B*", "*C*", "*D*") to 2 μm ("*B*", "*B*", "*C*", "*η*"), finally to 2.75 μm ("*B*", "*B*", none, "*B*"). If CNs are designed in visible wavelength, this characteristic can be further studied for color image coding and encryption.

4 Conclusion

In summary, we propose a new type of metasurface for generating multichannel hybrid polarization distribution in near-field. The units of our metasurfaces are cross-nanofin-shaped nano-WPs, which function as HWP, ±QWP, FDM WP or other retarders. The coding of these WP pixels enables multiple operation channels, where high-resolution grayscale image encryption, multi-image storage, or rapid polarization detection can be implemented by a single metasurface with broadband fidelity and high efficiency. The features of broadband, near-field modulation, polarization-/frequency-multiplexing and COMS compatible single layer manufacturing enrich the technology of metadevice design, and provide our CN coding pixels an enormous potential for further applications in imaging, polarization detection, quantum computing and communication. For example, interferences of multiphoton quantum state have been demonstrated through all-dielectric metasurface [31], and our CNs provide more flexible polarization controlling for quantum projection.

5 Materials and methods

5.1 Simulation

The numerical simulations are mainly performed by using three-dimensional finite difference time-domain (FDTD). The periodic boundary condition and perfectly matched layer are employed for the horizontal (*x*- and *y*-) and vertical (*z*-) directions in the simulation, respectively. The magnetic field distributions are simulated by finite integral technique, and the dielectric constant of silicon is taken from Palik model.

5.2 Optical Characterization

The measured transmissivities are obtained by the Fourier-transform infrared spectrometer (Vertex 80, Bruker) coupled with a confocal microscope (Hyperion 2000 IR). The infrared microscope pictures are shot by commercial infrared camera, MicronViewer MODEL 7290A. The bright/dark-field pictures are shot by commercial microscope, OLYMPUS MX50.

5.3 Nanofabrication

By using simple planar processes, the 2D patterns of cross-nanofins are directly defined on the commercial silicon wafer by electron beam lithography, and then by inductively coupled plasma reactive ion etching (ICP-RIE) process, the uncovered silicon areas are etched.

Author contributions: S.D. and Z.L. contributed equally to this work. S.D. and Z.L. conceived the experiment. S.D., C.S. and G.G. fabricated the samples. S.D., Z.L., and W.Z. performed the simulation and measurements. S.D. and Z.L. have drafted the work, and H.Y., J.L. and C.G. substantively revised it. All authors discussed the results and commented on the manuscript.

Research funding: This work was supported by the National Key Research and Development Program of China under Grant Nos. 2016YFA0200400, 2016YFA0200800, 2016YFA0300601; the National Natural Science Foundation of China under Grants Nos. 61888102, 11674387, 11974386, 61905274, and 12074420; Strategic Priority Research Program of the Chinese Academy of Sciences under Grant No. XDB33000000, XDB28000000, QYZDJ-SSW-SLH042.

Conflict of interest statement: The authors declare no competing financial interests.

References

[1] H.-H. Hsiao, C. H. Chu, and D. P. Tsai, "Fundamentals and applications of metasurfaces," *Small Methods*, vol. 1, p. 1600064, 2017.

[2] N. Yu and F. Capasso, "Flat optics with designer metasurfaces," *Nat. Mater.*, vol. 13, pp. 139–150, 2014.

[3] B. Xiong, L. Deng, R. Peng, and Y. Liu, "Controlling the degrees of freedom in metasurface designs for multi-functional optical devices," *Nanoscale Adv.*, vol. 1, pp. 3786–3806, 2019.

[4] X. Zang, F. Dong, F. Yue, et al., "Polarization encoded color image embedded in a dielectric metasurface," *Adv. Mater.*, vol. 30, p. 1707499, 2018.

[5] S. Sun, Z. Zhou, C. Zhang, et al., "All-dielectric full-color printing with TiO2 metasurfaces," *ACS Nano*, vol. 11, pp. 4445–4452, 2017.

[6] Y. Bao, Y. Yu, H. Xu, et al., "Coherent pixel design of metasurfaces for multidimensional optical control of multiple printing-image switching and encoding," *Adv. Funct. Mater.*, vol. 28, 2018, https://doi.org/10.1002/adfm.201870366.

[7] Y. Chen, X. Yang, and J. Gao, "3D Janus plasmonic helical nanoapertures for polarization-encrypted data storage," *Light Sci. Appl.*, vol. 8, p. 45, 2019.

[8] K. Chen, G. Ding, G. Hu, et al., "Directional janus metasurface," *Adv. Mater.*, vol. 32, p. e1906352, 2020.

[9] Y. Hu, X. Wang, X. Luo, et al., "All-dielectric metasurfaces for polarization manipulation: principles and emerging applications," *Nanophotonics*, vol. 9, pp. 3755–3780, 2020.

[10] Y. Intaravanne and X. Chen, "Recent advances in optical metasurfaces for polarization detection and engineered polarization profiles," *Nanophotonics*, vol. 9, pp. 1003–1014, 2020.

[11] C. Zhang, D. Wen, F. Yue, Y. Intaravanne, W. Wang, and X. Chen, "Optical metasurface generated vector beam for anticounterfeiting," *Phys. Rev. Appl.*, vol. 10, 2018, https://doi.org/10.1103/physrevapplied.10.034028.

[12] F. Yue, C. Zhang, X.-F. Zang, et al., "High-resolution grayscale image hidden in a laser beam," *Light Sci. Appl.*, vol. 7, p. 17129, 2017.

[13] C. Zhang, F. Dong, Y. Intaravanne, et al., "Multichannel metasurfaces for anticounterfeiting," *Phys. Rev. Appl.*, vol. 12, 2019, https://doi.org/10.1103/physrevapplied.12.034028.

[14] G. X. Zheng, H. Muhlenbernd, M. Kenney, G. X. Li, T. Zentgraf, and S. Zhang, "Metasurface holograms reaching 80% efficiency," *Nat. Nanotechnol.*, vol. 10, pp. 308–312, 2015.

[15] Q. Jiang, G. Jin, and L. Cao, "When metasurface meets hologram: principle and advances," *Adv. Opt. Photonics*, vol. 11, p. 518, 2019.

[16] Y. Hu, L. Li, Y. Wang, et al., "Trichromatic and tripolarization-channel holography with noninterleaved dielectric metasurface," *Nano Lett.*, vol. 20, pp. 994–1002, 2019.

[17] Z.-L. Deng, J. Deng, X. Zhuang, et al., "Diatomic metasurface for vectorial holography," *Nano Lett.*, vol. 18, pp. 2885–2892, 2018.

[18] J. P. B. Mueller, N. A. Rubin, R. C. Devlin, B. Groever, and F. Capasso, "Metasurface polarization optics: independent phase control of arbitrary orthogonal states of polarization," *Phys. Rev. Lett.*, vol. 118, 2017.

[19] A. Basiri, X. Chen, J. Bai, et al., "Nature-inspired chiral metasurfaces for circular polarization detection and full-Stokes polarimetric measurements," *Light Sci. Appl.*, vol. 8, p. 78, 2019.

[20] A. Arbabi, Y. Horie, M. Bagheri, and A. Faraon, "Dielectric metasurfaces for complete control of phase and polarization with subwavelength spatial resolution and high transmission," *Nat. Nanotechnol.*, vol. 10, pp. 937–943, 2015.

[21] M. Khorasaninejad and K. B. Crozier, "Silicon nanofin grating as a miniature chirality-distinguishing beam-splitter," *Nat. Commun.*, vol. 5, 2014, https://doi.org/10.1038/ncomms6386.

[22] A. C. Overvig, S. Shrestha, S. C. Malek, et al., "Dielectric metasurfaces for complete and independent control of the optical amplitude and phase," *Light Sci. Appl.*, vol. 8, p. 92, 2019.

[23] I. Staude and J. Schilling, "Metamaterial-inspired silicon nanophotonics," *Nat. Photonics*, vol. 11, pp. 274–284, 2017.

[24] S. Kruk, B. Hopkins, I. I. Kravchenko, A. Miroshnichenko, D. N. Neshev, and Y. S. Kivshar, "Broadband highly efficient dielectric metadevices for polarization control," *Apl Photonics*, vol. 1, 2016, https://doi.org/10.1063/1.4949007.

[25] L. Q. Cong, N. N. Xu, J. Q. Gu, R. Singh, J. G. Han, and W. L. Zhang, "Highly flexible broadband terahertz metamaterial quarter-wave plate," *Laser Photonics Rev.*, vol. 8, pp. 626–632, 2014.

[26] X. Li, L. Chen, Y. Li, et al., "Multicolor 3D meta-holography by broadband plasmonic modulation," *Sci. Adv.*, vol. 2, p. e1601102, 2016.

[27] M. Khorasaninejad, W. T. Chen, R. C. Devlin, J. Oh, A. Y. Zhu, and F. Capasso, "Metalenses at visible wavelengths: diffraction-limited focusing and subwavelength resolution imaging," *Science*, vol. 352, pp. 1190–1194, 2016.

[28] P. Lalanne, S. Astilean, P. Chavel, E. Cambril, and H. Launois, "Blazed binary subwavelength gratings with efficiencies larger than those of conventional échelette gratings," *Opt. Lett.*, vol. 23, pp. 1081–1083, 1998.

[29] Z. Zhu and T. Brown, "Full-vectorial finite-difference analysis of microstructured optical fibers," *Opt. Express*, vol. 10, pp. 853–864, 2002.
[30] M. Abramowitz and M. W. Davidson, "Specialized microscopy techniques – Darkfield Illumination," New York 1999, Available at: https://www.olympus-lifescience.com.cn/en/microscope-resource/primer/techniques/darkfield/.
[31] K. Wang, J. G. Titchener, S. S. Kruk, et al., "Quantum metasurface for multiphoton interference and state reconstruction," *Science*, vol. 361, pp. 1104–1108, 2018.

Supplementary Material: The online version of this article offers supplementary material (https://doi.org/10.1515/nanoph-2020-0621).